Journal of Computational Physics **154,** 174–196 (1999)
Article ID jcph.1999.6311, available online at http://www.idealibrary.com on IDEAL®

A Lagrangian–Eulerian Mapping Solver for Direct Numerical Simulation of Bubble-Laden Turbulent Shear Flows Using the Two-Fluid Formulation

O. A. Druzhinin[1] and S. E. Elghobashi

Department of Mechanical and Aerospace Engineering, University of California, Irvine, California 92697
E-mail: selghoba@uci.edu

Received February 18, 1999

In a recent study we showed that the two-fluid (TF) formulation can be used in the direct numerical simulation (DNS) of bubble- (or particle-) laden decaying isotropic turbulence with considerable saving in CPU-time and memory as compared to the trajectory approach employed by many researchers. In the present paper, we develop a Lagrangian–Eulerian mapping (LEM) solver for DNS of bubble-laden turbulent shear flows using TF. The purpose of LEM is to resolve the large gradients of bubble velocity and concentration which result from the absence of the diffusion terms in the equations of bubble-phase motion and the preferential accumulation of bubbles. A standard finite-difference scheme (FDS) fails to resolve these gradients. We examine the performance of the new method in DNS of a bubble-laden Taylor–Green vortex, spatially developing plane mixing layer, and homogeneous shear turbulent flow.

Key Words: particle-laden flows; two-fluid formulation; preferential accumulation; finite-difference scheme; integration along characteristics; Lagrangian–Eulerian mapping; bubble-laden flow; homogeneous shear turbulent flow.

I. INTRODUCTION

In a recent study [1] we used the two-fluid (TF) approach in direct numerical simulations (DNS) of a decaying isotropic turbulence laden with microbubbles. The TF approach treats each phase as a continuum with its own continuity and momentum equations. TF is an alternative to the trajectory approach commonly used in DNS of particle-laden flows [2]. The motivation for using TF in DNS of particle-laden flows is that it reduces considerably the required CPU-time and memory, as compared to the trajectory approach.

[1]On leave from Applied Physics Institute, Russian Academy of Sciences, 603600 Nizhni Novgorod, Russia.

0021-9991/99 $30.00

The implementation of TF formulation in DNS of particle- (or bubble-) laden turbulent shear flows may be limited by the large gradients of concentration of particles due to their preferential accumulation. Itis well known that heavy particles, due to their inertia, accumulate in the low-enstrophy regions of the flow [3–5]. On the other hand, bubbles with negligible mass but with added-mass inertia, accumulate in the high-enstrophy regions, generally associated with the centers of vortices [3]. This preferential accumulation creates regions devoid of bubbles neighboring regions of high bubble concentration and hence large gradients of concentration. The inability of a standard finite-difference scheme (FDS) to resolve these large gradients produces numerical instability and erroneous results. Another source of numerical instability is the presence of the nonlinear advection terms and the absence of the diffusion terms in the equation for the bubble-phase velocity. The nonlinear advection creates large gradients of bubble-phase velocity which are similar to those in the shock-wave solution of the inviscid Burgers equation [6]. The large gradients of the bubble velocity and concentration cause numerical resolution and stability problems when performing DNS with the TF formulation using FDS in solving the governing equations for the bubble-phase velocity and concentration.

In our study [1] we considered microbubbles, whose diameter, d_b, is smaller than the Kolmogorov length scale, η (to satisfy the necessary conditions for deriving the exact equations of bubble motion) and their response time, τ_b, is much smaller than the Kolmogorov time scale, τ_k. We showed that under these conditions, the preferential accumulation of bubbles in decaying isotropic turbulence is negligible. Thus, large gradients of bubble concentration and velocity are not created, and FDS can be successfully used in DNS/TF.

In the present paper, we develop a Lagrangian–Eulerian mapping solver (LEM) to perform DNS of bubble-laden flows using the TF formulation. The purpose of LEM is to resolve the large gradients of the bubble-phase velocity and concentration that are created by nonlinear advection and preferential accumulation in the absence of the diffusion terms in the equations of the bubble-phase motion. We examine the performance of LEM in DNS of three bubble-laden flows: Taylor–Green vortex, a plane spatially developing mixing layer, and a homogeneous shear turbulent flow. We consider bubbles with sufficiently large added-mass inertia and show that FDS is not capable of resolving the bubble-phase velocity and concentration, whereas LEM is.

The paper is organized as follows. The LEM solver is described in Section II. Section III examines the performance of LEM and compares it with that of FDS in DNS of a bubble-laden Taylor–Green vortex, a plane spatially developing mixing layer, and a homogeneous shear turbulent flow. Concluding remarks are presented in Section IV.

II. LAGRANGIAN–EULERIAN MAPPING SOLVER FOR A PARTICLE-LADEN FLOW

In this section we develop the LEM solver as a general method for the intergation of the conservation equations of mass and momentum of the dispersed phase (solid particles, liquid droplets, or gaseous bubbles). Hereinafter, the dispersed phase will be denoted as *particles*, unless stated otherwise. In the following sections, we examine the performance of LEM in DNS of bubble-laden flows only.

According to the two-fluid (TF) formulation [1], the conservation equations of the particle-phase momentum and mass can be written in the general form,

$$\partial_t V_i + V_j \partial_j V_i = F_i(\boldsymbol{V}, \boldsymbol{U}, \boldsymbol{r}, t), \tag{1}$$

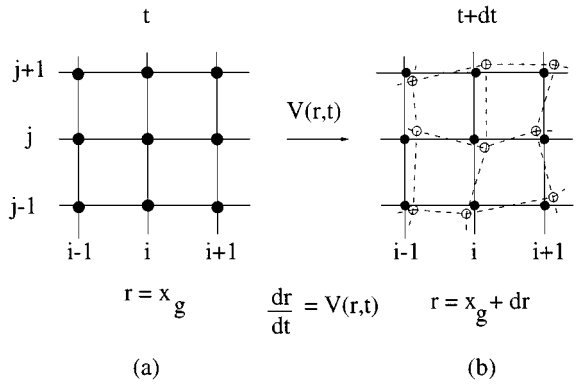

FIG. 1. Mapping of the Eulerian grid, $\boldsymbol{r}(t) = \boldsymbol{x}_g$, on the Lagrangian grid $\boldsymbol{r}(t + dt) = \boldsymbol{x}_g + d\boldsymbol{r}$. At time $t = 0$ the Lagrangian grid nodes (empty circles) coincide with the Eulerian grid nodes (filled circles in (a)). At time $t + dt$, the Lagrangian grid nodes are shifted with respect to the Eulerian grid nodes (b).

$$\partial_t C + \partial_j (C V_j) = 0, \tag{2}$$

where $\partial_t \equiv \partial/\partial t$ and $\partial_j \equiv \partial/\partial x_j$, and the term on the rhs of (1) describes the force acting on the particle. The fluid velocity, $\boldsymbol{U}(\boldsymbol{r}, t)$, at a given time t is assumed to be a known field obtained by the integration of the Navier–Stokes equations. $\boldsymbol{V}(\boldsymbol{r}, t)$ and $C(\boldsymbol{r}, t)$ are the particle-phase velocity and concentration, respectively.

As discussed earlier in the Introduction, large gradients of $\boldsymbol{V}$ and C are created due to the nonlinear advection as well as the preferential accumulation of particles and the absence of the diffusion terms in Eqs. (1) and (2). These large gradients often render a stable numerical solution of (1) and (2) impossible in DNS using a standard finite-difference scheme (FDS). In order to overcome this problem, we developed an Eulerian–Lagrangian mapping (LEM) solver to integrate Eqs. (1) and (2) for the particle velocity and concentration, as described below.

At a given time step, t, the fields $C(\boldsymbol{r}, t)$, $\boldsymbol{V}(\boldsymbol{r}, t)$, and $\boldsymbol{U}(\boldsymbol{r}, t)$ are defined at the Eulerian grid nodes with coordinates $\boldsymbol{r} = \boldsymbol{x}_g$, where $\boldsymbol{x}_g = \{i\Delta x, j\Delta x, k\Delta x\}$, $i = 1, \ldots, N$, $j = 1, \ldots, N$, $k = 1, \ldots, N$, $\Delta x = 1/N$ (Fig. 1). In order to obtain the velocity, $\boldsymbol{V}(\boldsymbol{x}_g, t + dt)$, and concentrations, $C(\boldsymbol{x}_g, t + dt)$, at the next time step $(t + dt)$ at the *same* Eulerian grid nodes, $\boldsymbol{x}_g$, the LEM solver proceeds as follows.

First, the time integration of Eqs. (1) and (2) is performed along the characteristics $\boldsymbol{r}(t)$, which are defined via

$$\frac{d\boldsymbol{r}}{dt} = \boldsymbol{V}(\boldsymbol{r}, t), \tag{3}$$

with the initial condition at time t,

$$\boldsymbol{r}(t) = \boldsymbol{x}_g. \tag{4}$$

The velocity $\boldsymbol{V}(\boldsymbol{r}(t + dt), t + dt)$ is then evaluated via a predictor-corrector scheme as

$$\begin{aligned} \boldsymbol{V}^* &= \boldsymbol{V}(\boldsymbol{x}_g, t) + dt\, \boldsymbol{F}(\boldsymbol{x}_g, t), \\ \boldsymbol{V}(\boldsymbol{r}(t + dt), t + dt) &= \boldsymbol{V}(\boldsymbol{x}_g, t) + \frac{1}{2} dt (\boldsymbol{F}^* + \boldsymbol{F}(\boldsymbol{x}_g, t)), \end{aligned} \tag{5}$$

where

$$\boldsymbol{F}^* = \boldsymbol{F}(\boldsymbol{U}, \boldsymbol{V}^*, \boldsymbol{x}_g, t). \tag{6}$$

The concentration, $C(\boldsymbol{r}(t+dt), t+dt)$, is also evaluated via a predictor-corrector scheme as

$$\begin{aligned} C^* &= C(\boldsymbol{x}_g, t) - dt\, C(\boldsymbol{x}_g, t)\,\mathrm{div}\,\boldsymbol{V}(\boldsymbol{x}_g, t), \\ C(\boldsymbol{r}(t+dt), t+dt) &= C(\boldsymbol{x}_g, t) - \frac{1}{2}dt[C(\boldsymbol{x}_g, t) + C^*]\,\mathrm{div}\,\boldsymbol{V}(\boldsymbol{x}_g, t). \end{aligned} \tag{7}$$

Now the velocity, $\boldsymbol{V}$, and concentration, C, are defined via Eqs. (5) and (7) at Lagrangian grid nodes with coordinates $\boldsymbol{r}(t+dt)$ given by

$$\boldsymbol{r}(t+dt) = \boldsymbol{x}_g + d\boldsymbol{r}, \tag{8}$$

where the displacement $d\boldsymbol{r}$ is obtained by time integration of Eq. (3) as

$$d\boldsymbol{r} = \frac{1}{2}dt[\boldsymbol{V}(\boldsymbol{r}(t+dt), t+dt) + \boldsymbol{V}(\boldsymbol{x}_g, t)], \tag{9}$$

with the initial condition (4). Equations (3), (4), (8), and (9) define a mapping of the Eulerian grid, $\boldsymbol{x}_g$, onto a Lagrangian grid, $\boldsymbol{x}_g + d\boldsymbol{r}$ (see Fig. 1). Now the desired velocity and concentration can be evaluated at the Eulerian grid nodes via interpolation.

In order to retain the second-order accuracy of the solver, we prescribe the time step, dt, small enough, so that

$$u_0 dt \sim (\Delta x)^2, \tag{10}$$

where u_0 is a characteristic magnitude of the velocity field $\boldsymbol{U}$ (e.g., turbulence rms velocity). Then, the displacement modulus $|d\boldsymbol{r}| \simeq u_0 dt$, and

$$|d\boldsymbol{r}| \sim (\Delta x)^2. \tag{11}$$

Note also that, for $\Delta x \ll 1$, (10) ensures that the CFL stability condition is satisfied in the integration of the Navier–Stokes equations for the fluid velocity.

Now we obtain the particle concentration, $C(\boldsymbol{x}_g, t+dt)$, and velocity $\boldsymbol{V}(\boldsymbol{x}_g, t+dt)$, at the Eulerian grid nodes ($\boldsymbol{x}_g$) using fields $C(\boldsymbol{r}(t+dt), t+dt)$ and $\boldsymbol{V}(\boldsymbol{r}(t+dt), t+dt)$, defined at the Lagrangian grid nodes ($\boldsymbol{r}(t+dt)$), (8) via

$$C(\boldsymbol{x}_g, t+dt) = (1 - d\boldsymbol{r}\nabla)C(\boldsymbol{r}(t+dt), t+dt), \tag{12}$$

and

$$\boldsymbol{V}(\boldsymbol{x}_g, t+dt) = (1 - d\boldsymbol{r}\nabla)\boldsymbol{V}(\boldsymbol{r}(t+dt), t+dt). \tag{13}$$

It should be noted that the interpolation (12) makes LEM a non-conservative scheme. Thus the concentration gradient, defined in (12) on the Lagrangian grid (8) with non-uniform spacings, should be evaluated with sufficient accuracy. In the DNS of bubble-laden flows presented in the next section, the gradients of the concentration and velocity are evaluated using the corresponding values at the Lagrangian grid nodes via central finite differencing as

$$\nabla_i C = \frac{C(i+1, j, k, t+dt) - C(i-1, j, k, t+dt)}{2\Delta x} \tag{14}$$

and

$$\nabla_i \boldsymbol{V} = \frac{\boldsymbol{V}(i+1, j, k, t+dt) - \boldsymbol{V}(i-1, j, k, t+dt)}{2\Delta x} \tag{15}$$

in a given (ith) direction.

The calculations of the gradients of the velocity and concentration via Eqs. (14) and (15) are of second-order accuracy in Δx due to condition (11). Thus, for $(\Delta x)^2 \sim |d\boldsymbol{r}|$, the interpolation (12)–(15) does not degrade the over-all second-order (both in space and time) accuracy of the LEM solver.

III. VALIDATION OF LEM SOLVER FOR BUBBLE-LADEN FLOWS

In this section we present the results of DNS using LEM for three different flows laden with small spherical bubbles: a Taylor–Green vortex, a two-dimensional spatially developing mixing layer, and a three-dimensional homogeneous shear turbulent flow. Our objective is to examine the performance of DNS using LEM and to compare the results with those obtained from DNS using a standard finite-difference scheme (FDS).

We employ TF for the equations of motion of the bubble-phase, and the same assumptions and physical properties of the bubbles (the bubble gas density and the boundary condition at the bubble surface) as in our earlier study [1].

A. *Bubble-Laden Taylor–Green Vortex*

As a first test case, we consider a Taylor–Green vortex (TG) flow laden with bubbles. We assume that the bubble concentration is small enough, so that they do not affect the carrier flow (one-way coupling). The governing equations of the conservation of the momentum and mass for the fluid and bubble phases are [1]:

fluid phase,

$$\frac{DU_i}{Dt} = -\frac{1}{\rho_f}\partial_i P + \nu \Delta U_i, \tag{16}$$

$$\partial_j U_j = 0; \tag{17}$$

bubble phase,

$$\frac{dV_i}{dt} = 3\frac{DU_i}{Dt} + \frac{1}{\tau_b}(U_i - V_i), \tag{18}$$

$$\frac{dC}{dt} = -C\partial_j V_j. \tag{19}$$

In the above equations, V_i and U_i are the instantaneous velocities of the bubble-phase and fluid, and C is the instantaneous bubble concentration. The notations for the total derivatives are $D/Dt = \partial_t + U_j\partial_j$ and $d/dt = \partial_t + V_j\partial_j$. The bubble response time τ_b is

$$\tau_b = \frac{d_b^2}{36\nu}. \tag{20}$$

In this test simulation we neglect the effect of the gravity.

TG-flow [7] represents an exact two-dimensional, time-dependent solution of the Navier–Stokes equations (16) and continuity equation (17) with the velocity components (U_x, 0, U_z). The corresponding instantaneous, local stream function can be written as

$$\Psi(x, z, t) = \frac{\omega_0}{k^2} \exp(-\nu k^2 t) \cos k_x x \cos k_z z, \tag{21}$$

where ω_0 is the initial maximum vorticity; k_x and k_z are the wave numbers in x and z directions, and $k^2 = k_x^2 + k_z^2$. The flow vorticity, ω, and pressure, P, are

$$\omega = \frac{\partial U_x}{\partial z} - \frac{\partial U_z}{\partial x} = -k^2 \Psi, \tag{22}$$

$$P = P_0 - \frac{1}{2}\left[\left(\frac{\partial \Psi}{\partial x}\right)^2 + \left(\frac{\partial \Psi}{\partial z}\right)^2 + k^2 \Psi^2\right]. \tag{23}$$

The fluid velocity components are

$$U_x = \frac{\partial \Psi}{\partial z} = -\omega_0 \frac{k_z}{k^2} \exp(-\nu k^2 t) \cos k_x x \sin k_z z, \tag{24}$$

$$U_z = -\frac{\partial \Psi}{\partial x} = \omega_0 \frac{k_x}{k^2} \exp(-\nu k^2 t) \sin k_x x \cos k_z z. \tag{25}$$

DNS is performed for a flow Reynolds number $Re = 1/\nu = 10000$, and an initially uniform concentration of bubbles. We set the parameters $k_x = k_z = 2\pi$ and $\omega_0 = 1$. The initial fluid pressure and velocity are prescribed by Eqs. (23), (24), and (25) at $t = 0$. The initial velocity components V_x and V_z of the bubble phase are set equal to those of the surrounding fluid, and the initial bubble concentration is uniform constant,

$$V_x = U_x, \qquad V_z = U_z, \qquad C = \alpha_0, \tag{26}$$

where α_0 is small enough (e.g., $\alpha_0 = 10^{-4}$) to neglect the influence of the bubbles on the carrier flow as well as the direct interaction between the bubbles.

DNS is performed with two different grids of $96 \times 4 \times 96$ and $192 \times 4 \times 192$ points in the x, y, and z directions, and for two bubble response times, $\tau_b = 0.15$ and 0.45. Although the TG flow considered here is essentially two-dimensional, the numerical method uses a 3D-algorithm, where the flow is homogeneous in y-direction. The integration is performed with time step $\Delta t = 0.5\Delta x$, where cell size $\Delta x = 1/N_g$ and $N_g = 96$ or 192 for the two different meshes.

Figure 2 shows the contours of the enstrophy, ω^2, and bubble concentration, C (in gray scale) in an (x, z)-plane obtained from DNS using LEM solver with mesh $192 \times 4 \times 192$ at time $t = 20$ for $\tau_b = 0.45$. The figure shows that, owing to the inertial bias, the bubbles accumulate at the vortex centers (e.g., points $(x = 0, z = 0)$ and $(x = 0.5, z = 0.5)$). Consequently, local sharp peaks of the bubble concentration are created at the vortex centers, where the enstrophy has its local maxima.

The growth of the bubble concentration at the vortex center can be described analytically provided that the bubble response time is small compared to the flow time scale, i.e., $(\tau_b/\tau_f)^2 \simeq (\tau_b \omega_0)^2 \ll 1$. Then, an approximate solution of Eq. (19) for the maximum bubble

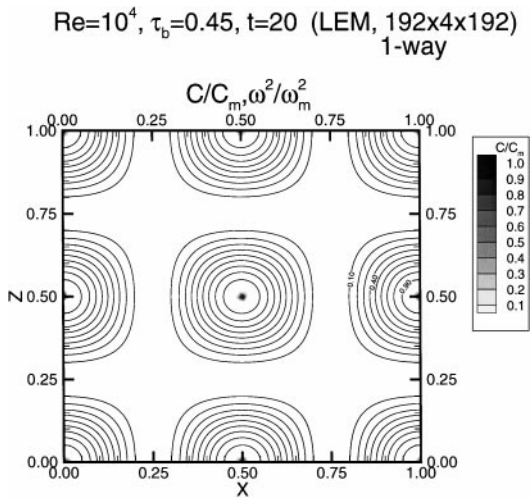

FIG. 2. Contours of the flow enstrophy, ω^2/ω_m^2 (in lines), and bubble concentration, C/C_m (in grey scale), normalized by the corresponding maximum values, $\omega_m^2 = 0.788$ and $C_m/\alpha_0 = 752$, in the Taylor–Green vortex flow at time $t = 20$. The increments of the enstrophy contours are equal to those in the table for the concentration.

concentration, C_m, at the vortex center, can be written in the form [1]

$$C_m = \alpha_0 \exp\left\{ \frac{2\tau_b}{\nu} \left(\omega_0 \frac{k_x k_z}{k^3} \right)^2 [1 - \exp(-2\nu k^2 t)] \right\}. \tag{27}$$

Figure 3a compares the temporal development of the bubble concentration at the vortex center, $C_m(t)$, normalized by the reference concentration α_0, obtained from the analytical solution (27) for $\tau_b = 0.15$ to that of DNS using LEM solver (with meshes $96 \times 4 \times 96$ and $192 \times 4 \times 192$) and DNS using FDS (with mesh $96 \times 4 \times 96$). As expected (for $(\tau_b \omega_0)^2 = 0.0225 \ll 1$), the figure shows good agreement between the DNS results and the analytical solution (27). Also, the difference between the DNS/LEM results of the two meshes is less than 1%.

In the case of relatively small bubbles ($\tau_b \omega_0 \leq 0.15$), no numerical instability is observed in DNS using FDS for $t \leq 15$. However, the instability occurs for larger τ_b, when the preferential bubble accumulation becomes more pronounced. Figure 3b compares the temporal development of the concentration maximum and minimum, C_{max} and C_{min}, obtained in DNS using LEM and FDS for $\tau_b = 0.45$. The figure shows that, for $t > 10$, FDS reduces the growth rate of C_{max} as compared to LEM. The figure also shows that the numerical instability develops in DNS with FDS for $t > 15$, causing an exponential growth of negative C_{min} which is unacceptable. On the other hand, no numerical instability occurs in DNS using LEM. The bubble concentration distribution obtained in DNS using LEM at time $t = 20$ is presented in Fig. 2. In this case, the difference between the results for C_{max} from the DNS/LEM with two different meshes ($96 \times 4 \times 96$ and $192 \times 4 \times 192$) is of the order of 5% (cf. Fig. 3b). Thus, in our DNS using LEM the effect of numerical diffusion remains negligible.

As was discussed in Subsection A, LEM solver is not a conservative scheme. Therefore, as the concentration gradients grow, the conservation of the volume integral of C over the computational domain (evaluated as a sum over all grid nodes) should be checked. In the present test case, this quantity is conserved with an accuracy of 0.1% in the simulation with $\tau_b = 0.15$ and 3% in the simulation with $\tau_b = 0.45$.

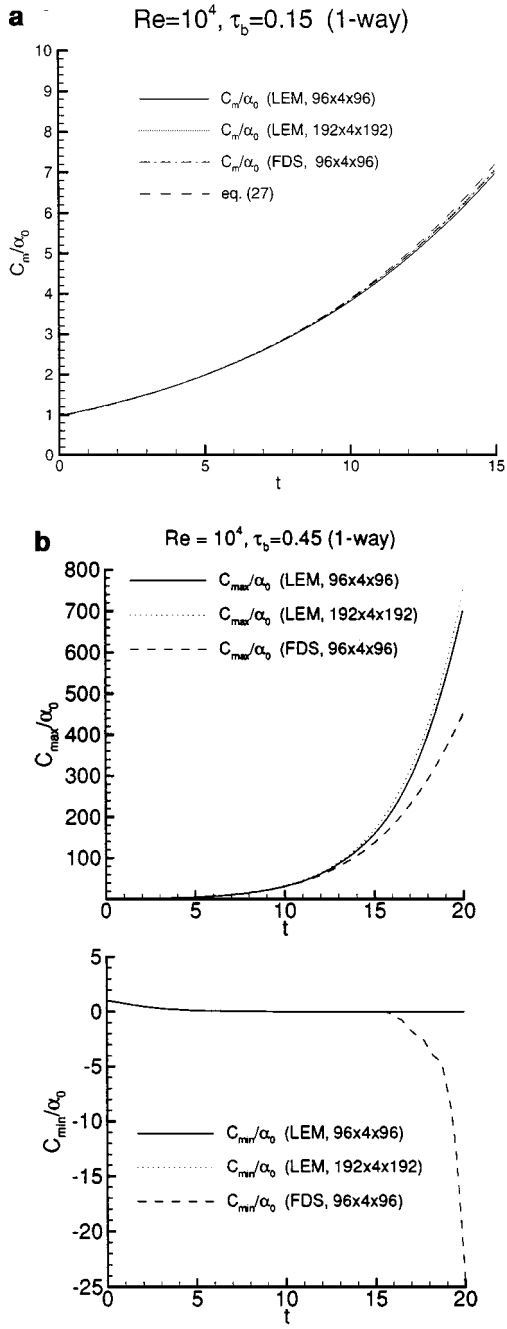

FIG. 3. (a) Temporal development of the maximum bubble concentration in the DNS with LEM solver (for different meshes) and FDS of the bubble-laden Taylor–Green vortex; bubble response time $\tau_b = 0.15$. The analytical solution for the concentration at the vortex center is in the dashed line. (b) Temporal development of the maximum and minimum values, C_{max} and C_{min}, of the bubble concentration in the DNS of the bubble-laden Taylor–Green vortex with LEM solver (for different meshes) and FDS; $\tau_b = 0.45$.

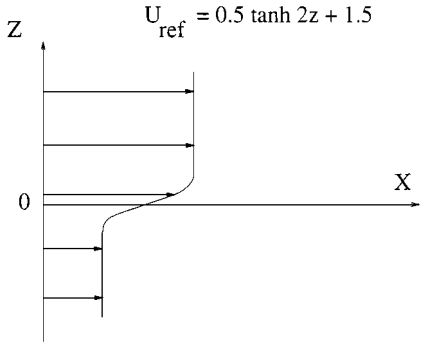

FIG. 4. Reference frame and the inflow streamwise velocity profile for a spatially developing plane mixing layer (SDML).

B. *Bubble-Laden Spatially Developing Mixing Layer*

Here we test LEM in a two-dimensional spatially developing mixing layer (SDML), laden with small concentration of bubbles (one-way coupling). In a recent study [8] we developed a numerical procedure and performed DNS/LEM of a three-dimensional bubble-laden SDML. Thus in the present paper we consider the two-dimensional case only and show that FDS is not capable of resolving the bubble-phase velocity and concentration in this flow, whereas LEM is.

Figure 4 shows the flow geometry and reference frame. The inflow reference streamwise fluid velocity profile, $U_{ref}(z)$, at $x = 0$ is prescribed as (Fig. 4)

$$U_{ref}(z) = 0.5 \tanh 2z + 1.5. \tag{28}$$

In this case, all the variables are made dimensionless via scaling by the initial vorticity thickness, $\delta^*_{\omega 0}$, and velocity difference, $U^*_+ - U^*_- = \Delta U^*$, where U^*_+ and U^*_- are the velocities of the high- and low-speed streams. The corresponding dimensionless velocities (obtained as $U^\pm = U_{ref}(z \to \pm\infty)$) are $U^+ = 2$ and $U^- = 1$, and the initial dimensionless vorticity thickness is

$$\delta_{\omega 0} = \left.\frac{\Delta U}{dU_{ref}/dz}\right|_{z=0} = 1. \tag{29}$$

In this case, the governing dimensionless equations of the conservation of the momentum and mass for the fluid and bubble phases are:

fluid,

$$\frac{D\tilde{U}_i}{Dt} + U_{ref}\,\partial_x \tilde{U}_i + \tilde{U}_z \delta_{ix} \frac{dU_{ref}}{dz} = -\frac{1}{\rho_f}\partial_i P + \nu\left(\delta_{ix}\frac{d^2 U_{ref}}{dz^2} + \partial^2 \tilde{U}_i\right), \tag{30}$$

$$\partial_j \tilde{U}_j = 0; \tag{31}$$

bubble phase,

$$\frac{d\tilde{V}_i}{dt} + U_{ref}\,\partial_x \tilde{V}_i + \tilde{V}_z \delta_{ix} \frac{dU_{ref}}{dz} = 3\left(\frac{D\tilde{U}_i}{Dt} + U_{ref}\,\partial_x \tilde{U}_i + \tilde{U}_z \delta_{ix} \frac{dU_{ref}}{dz}\right) + \frac{1}{\tau_b}(\tilde{U}_i - \tilde{V}_i + W\delta_{iz}), \tag{32}$$

$$\frac{dC}{dt} + U_{ref}\,\partial_x C = -C\,\partial_j \tilde{V}_j. \tag{33}$$

In the above equations, $\tilde{U}_i$ and $\tilde{V}_i$ are the deviations of the instantaneous fluid and bubble-phase velocities from the reference profile U_{ref}. The dimensionless viscosity is set equal to $\nu = 1/Re$ where $Re = \Delta U^* \delta^*_{\omega 0}/\nu^*$ is the Reynolds number based on the dimensional velocity difference ΔU^*, the initial vorticity thickness, $\delta^*_{\omega 0}$, and fluid kinematic viscosity, ν^*. The notations for the total derivatives D/Dt and d/dt are similar to those in Eqs. (16)–(19), and the bubble response time, τ_b, is defined in (20). The bubble terminal velocity, W, is defined as

$$W = 2\tau_b g, \tag{34}$$

where g is the projection of the dimensionless gravity acceleration on the z- axis, $g_i = -g\delta_{iz}$. In our DNS, we prescribe $g = 1$.

1. Numerical method for the carrier flow. In order to perform DNS in a finite computational domain which corresponds to a physical domain infinite in the vertical (z) direction (Fig. 4), and to resolve the mixing layer core zone with sufficient accuracy, a mapping for z-coordinate is introduced in the form

$$\xi = \tanh\frac{z}{8}, \tag{35}$$

and

$$z = 4\ln\left(\frac{1+\xi}{1-\xi}\right), \tag{36}$$

so that $-1 \le \xi \le 1$ corresponds to $-\infty < z < \infty$. Thus, the partial derivatives with respect to z in Eqs. (30)–(33) are expressed as

$$\frac{\partial}{\partial z} = \left(\frac{1-\xi^2}{8}\right)\frac{\partial}{\partial \xi}. \tag{37}$$

Accordingly, the reference velocity (28) and its first and second derivatives are obtained as explicit functions of ξ according to (35) and the equality ($\tanh 2z = 2\tanh z/(1+\tanh^2 z)$).

Although the flow is uniform in the y-direction, we use a three-dimensional numerical procedure, developed in our recent study [8], to solve the momentum conservation and continuity equations (30)–(33) in a parallelpiped computational domain whose dimensionless sides are $0 \le x \le 80$, $0 \le y \le 0.667$, and $-1 \le \xi \le 1$. Equations (30) and (31) for the fluid phase are discretized in an Eulerian framework using a second-order finite-differencing on an equispaced staggered grid containing $N_x = 480$ points in the x-direction, $N_y = 4$ in the y-direction, and $N_z = 96$ in the $z(\xi)$-direction.

The mean advection terms, $U_{ref}\,\partial_x \tilde{U}_i$, are evaluated using a second-order upwind differencing scheme [9]. A second-order Adams–Bashforth scheme is used to integrate the equations in time. Pressure is obtained by solving its Poisson equation via a cosine transform (employing FFT [10, 11]) in the x-direction, using FFT in the y-direction, and Gaussian elimination in the $z(\xi)$-direction [12].

Standard periodic boundary conditions for the velocity components, pressure, and the bubble concentration are imposed in the spanwise (y) direction. The Neumann's (stress-free) conditions are imposed in the $z(\xi)$-direction as

$$\frac{\partial \phi}{\partial \xi} = 0, \qquad \text{at } \xi = \pm 1, \tag{38}$$

where ϕ denotes the bubble and fluid velocities, pressure, and the concentration.

Two different boundary conditions are imposed in the streamwise (x) direction, at the inflow ($y-z$) plane, $x=0$, and outflow plane, $x=80$.

At the inflow plane ($x=0$), forcing is used to initialize the spanwise vortex rollup [9]. Thus the unsteady fluid velocity components at $x=0$, $U_x^f(z,t)$ and $U_z^f(z,t)$, are composed of the product of harmonic functions of time and the eigenfunctions of the most unstable (fundamental) model with frequency $\Omega_0 = 4/3$, and its first and second subharmonics, $\Omega_{1,2}$. The eigenfunctions are obtained by solving the two-dimensional Rayleigh-equation eigenvalue problem for each of the three frequencies $\Omega_{0,1,2}$. We follow the proposal of Sandham and Reynolds [13] and include random-walk phases in the forcing functions to simulate a natural mixing layer. All modes are forced at an amplitude of 0.02.

The inflow bubble concentration is uniform constant, $C(x=0, y, z) = \alpha_0$, and the inflow bubble velocity is set equal to the instantaneous local fluid inflow velocity.

At the outflow plane ($x=80$), a time-dependent, advection condition is imposed as

$$\partial_t \phi + U_a \partial_x \phi = 0, \tag{39}$$

where ϕ denotes the velocities $\tilde{U}_i$, $\tilde{V}_i$, and concentration C, and $U_a = (U^+ + U^-)/2 = 1.5$ is the nominal speed of the vortex structures [9] (defined as an average of the high- and low-speed stream velocities, $U^+ = 2$ and $U^- = 1$).

2. Testing LEM solver in DNS of the bubble-laden SDML. We integrate Eqs. (32) and (33) in two steps. First, we integrate (32) and (33) using LEM solver, without taking into account the advection terms due to the reference velocity, $U_{ref}\partial_x \tilde{V}_i$ and $U_{ref}\partial_x C$. The resulting equations are

$$\frac{d\hat{V}_i}{dt} = -\tilde{V}_z \delta_{ix} \frac{dU_{ref}}{dz} + 3\left(\frac{D\tilde{U}_i}{Dt} + U_{ref}\partial_x \tilde{U}_i + \tilde{U}_z \delta_{ix} \frac{dU_{ref}}{dz} \right) + \frac{1}{\tau_b}(\tilde{U}_i - \tilde{V}_i + W\delta_{iz}), \tag{40}$$

$$\frac{d\hat{C}}{dt} = -C\partial_j \tilde{V}_j, \tag{41}$$

where $\hat{V}_i$ and $\hat{C}$ denote the intermediate values of bubble-phase velocity and concentration, respectively.

At the second step, we account for the advection terms due to the reference velocity, i.e., the second term on the lhs of both Eqs. (32) and (33). Thus we evaluate the bubble velocity, $\tilde{\boldsymbol{V}}$, and concentration, C, at the upstream position from where they are advected by the mean velocity U_{ref} (in the x-direction) during the time step dt as

$$\tilde{V}_i = \hat{V}_i - U_{ref}\partial_x \hat{V}_i dt, \tag{42}$$

and

$$C = \hat{C} - U_{ref}\,\partial_x \hat{C}\,dt, \tag{43}$$

where the gradients of $\hat{V}_i$ and $\hat{C}$ are evaluated via a second-order upwind differencing [9].

DNS of SDML is performed for Reynolds number $Re = 400$ with time step $\Delta t = 0.1\Delta x = 1/60$. The instantaneous fluid velocity field, $\tilde{U}_i$, $i = x, y, z$, at time $t = 0$ is set equal to zero throughout the computational domain. In order to minimize the influence of the initial conditions and the transient fluid motion, we compute only the fluid velocity field until time $t = 80$ from Eqs. (30) and (31). By this time, the initial flow-field is "washed" out of the computational domain by the mean advection, and the carrier flow can be regarded as nearly stationary. At $t = 80$ we inject bubbles into the flow and start solving Eqs. (32) and (33) for the bubble-phase velocity and concentration together with Eqs. (30) and (31) for the carrier fluid velocity. The initial bubble concentration is uniform constant throughout the computational domain, $C(t = 0) = \alpha_0$, where α_0 is small enough to neglect the influence of the bubbles on the carrier flow (e.g., $\alpha_0 = 10^{-4}$).

The bubble response time is prescribed as $\tau_b = 0.05$. Thus the dimensionless bubble diameter, $d_b = (36\nu\tau_b)^{1/2} \simeq 0.015$, where $\nu = 1/Re$, $Re = 400$, so that the condition $d_b \ll \delta_{\omega 0} = 1$ is satisfied. The dissipation length scale of the flow, l_{diss}, is estimated as $l_{diss} \simeq 1/(Re\,\omega_{max})^{1/2}$. The vorticity maximum is of the order $\omega_{max} \simeq 1$ throughout the simulation, so that $l_{diss} \simeq 0.05$. Therefore, the bubble diameter is smaller than the flow dissipation scale, and much smaller than the initial layer vorticity thickness; $d_b < l_{diss} \ll \delta_{\omega 0}$. Thus the two-fluid formulation is justified in this case. Our numerical results show that the bubble Reynolds number remains less than 1 throughout the simulation. The conditions $Re_b < 1$ and $d_b < l_{diss}$ are consistent with the assumptions used in deriving the equation of motion of the bubble phase (32).

The initial bubble velocity at any location is set equal to the local instantaneous fluid velocity,

$$\tilde{V}_i = \tilde{U}_i. \tag{44}$$

Figure 5 compares the temporal development of the absolute instantaneous maxima of the modulus of the divergence of the bubble velocity, $|\mathrm{div}\,\boldsymbol{V}|_m$, and the concentration gradient, $|\nabla C|_m$, obtained from DNS with LEM and FDS. The figure shows that in the DNS with FDS, numerical instability in the velocity of the bubble phase develops shortly after the injection of bubbles into the flow. The instability is first manifested in the exponential growth of $|\mathrm{div}\,\boldsymbol{V}|_m$ (for $t \simeq 80.15$) and consequently causes an explosive growth of $|\nabla C|_m$ for $t > 80.5$. Thus, in this flow, the *nonlinear advection* of the bubble velocity and the absence of the diffusion terms on the rhs of Eq. (32) triggers the instability. Note also that applying random phases in the forcing at the inflow plane ($x = 0$), $U_x^f(z, t)$ and $U_z^f(z, t)$, facilitates the development of the instability in DNS using FDS. On the other hand, DNS using LEM does not suffer from any numerical instability (cf. Fig. 5).

Figure 6a shows the instantaneous contours of ω_y, the y-component of the vorticity (in grey scale) at three different times, $t = 85$ (i), $t = 90$ (ii), and $t = 95$ (iii). This vorticity component, ω_y, is obtained from the instantaneous fluid velocity field $\tilde{U}_i$ according to

$$\omega_y = \frac{dU_{ref}}{dz} + \partial_z \tilde{U}_x - \partial_x \tilde{U}_z. \tag{45}$$

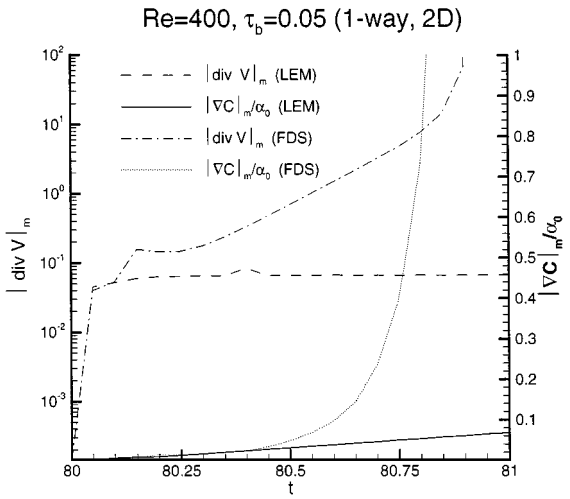

FIG. 5. Temporal development of the maxima of the modulus of the divergence of bubble velocity, $|\mathrm{div}\,\boldsymbol{V}|_m$, and the concentration gradient, $|\nabla C|_m/\alpha_0$, in the DNS with FDS and LEM of the bubble-laden SDML.

The figure shows the vortex pairing and rollup, enhanced by forcing at the subharmonic frequency Ω_1. Comparing the locations of the rollers in Fig. 3 ((i)–(iii)) shows that the rollers are advected with velocity $U_a = 1.5$. Note also that the vortices exit the domain naturally, without being distorted, thus confirming the accuracy of the advection boundary condition (39) at the outflow plane ($x = 80$).

Figure 6b shows the bubble concentration obtained in DNS with LEM for the same times ($t = 85, 90, 95$) as in Fig. 3a. The figure shows that bubbles, due to their added-mass inertia, accumulate in the centers of the (ω_y) rollers. In this simulation, the intergal of the bubble concentration C over the computational domain is conserved with accuracy $\simeq$0.1%.

C. *Bubble-Laden Homogeneous Shear Turbulent Flow*

The results of DNS of bubble-laden TG and SDML in the preceding sections show that LEM is capable of capturing the effects of the bubble preferential accumulation without creating numerical instabilities. As a further validation of the performance of LEM, we study in this section a bubble-laden homogeneous shear turbulent flow (HSF). The homogeneous shear is implemented via prescribing a mean fluid velocity $U_{ref} = (Sz, 0, 0)$, where S is the dimensionless velocity gradient in the z-direction. We consider both one-way and two-way coupling cases, where the latter allows the bubble-phase motion to affect that of the fluid.

The dimensionless equations of the conservation of momentum and mass for the fluid and bubble phases are [1]:

fluid phase,

$$\frac{DU_i}{Dt} + Sz\partial_x U_i + U_z S\delta_{ix} = -\frac{1}{\rho_f}\partial_i \tilde{P} + \nu\Delta U_i + C' g\delta_{iz}, \tag{46}$$

$$\partial_j U_j = 0; \tag{47}$$

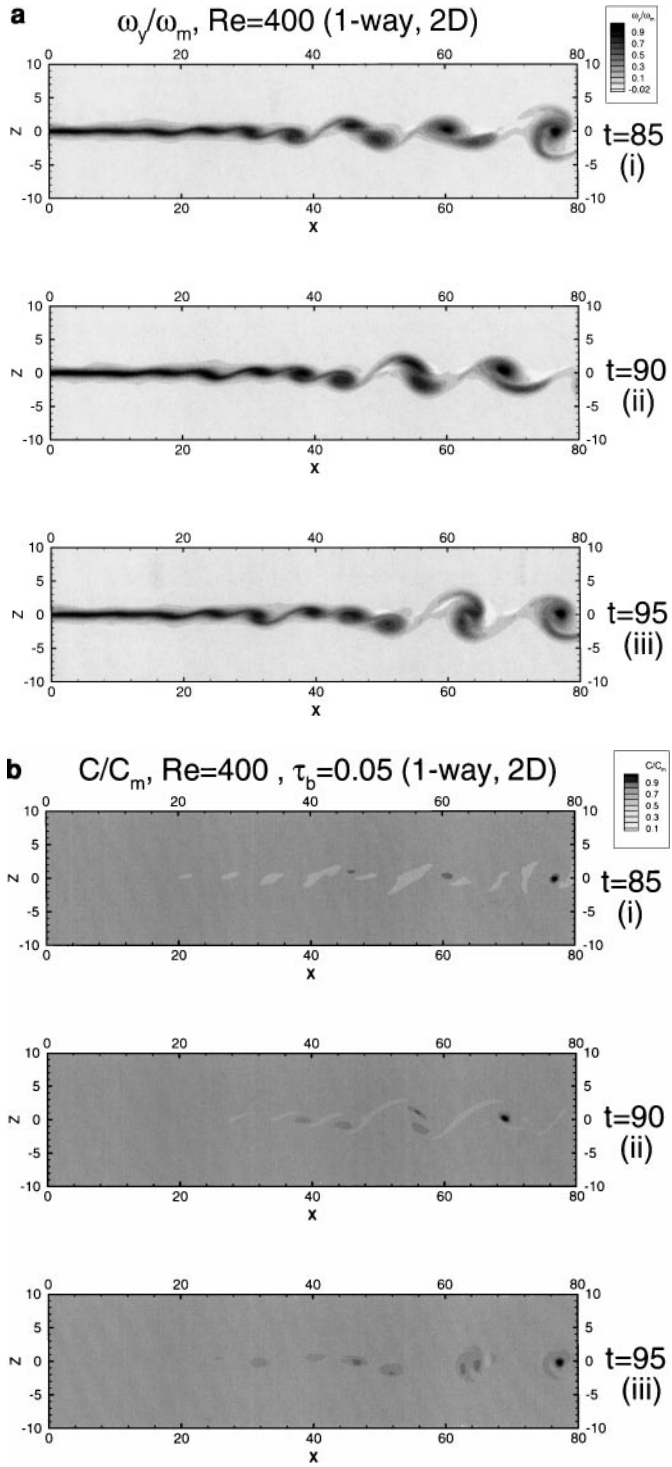

FIG. 6. (a) ω_y-vorticity contours of the two-dimensional spatially developing mixing layer at different times, $t = 85$ (i), $t = 90$ (ii), and $t = 95$ (iii). Vorticity maxima are $\omega_m = 1.14$, 1.03, and 1.12, respectively. (b) Bubble concentration contours in the two-dimensional spatially developing mixing layer at different times, $t = 85$ (i), $t = 90$ (ii), and $t = 95$ (iii). Concentration maxima are $C_m = 1.4\alpha_0$ (i), $C_m = 1.6\alpha_0$ (ii), and $C_m = 2.12\alpha_0$ (iii), respectively.

bubble phase,

$$\frac{dV_i}{dt} + Sz\partial_x V_i + V_z S\delta_{ix} = 3\left(\frac{DU_i}{Dt} + Sz\partial_x U_i + U_z S\delta_{ix}\right) + \frac{1}{\tau_b}(U_i - V_i + W\delta_{iz}), \quad (48)$$

$$\frac{dC'}{dt} + Sz\partial_x C' = -(C' + C_0)\partial_j V_j - S_C(V_z - W). \quad (49)$$

In the above equations, U_i and V_i are the deviations of the instantaneous fluid and bubble-phase velocities from the reference mean profile, $U_{ref}(z)$, and C' is the instantaneous deviation of the bubble concentration, C, from the instantaneous mean concentration in a given $(x-y)$ plane, $C_0(z,t)$, i.e.,

$$C' = C - C_0(z,t). \quad (50)$$

The modified hydrostatic part of the pressure field, $\tilde{P}$ in Eq. (46) is defined by using the analogy between the bubbly flow and a stratified flow with density $(1 - C_0(z,t))\rho_f$,

$$\tilde{P} = P + \rho_f g \int_0^z (1 - C_0)\, dz, \quad (51)$$

where P is the dynamic pressure. The initial reference bubble concentration, $C_0(z,0)$, is either uniform or has a constant gradient, i.e., $\partial_z C_0 = S_C$, where $S_C = -1$, 0, and $+1$. Thus, the instantaneous mean concentration $C_0(z,t)$ can be obtained by manipulating Eq. (49) and the transport equation of $C(\boldsymbol{r},t)$ according to

$$C_0(z,t) = C_0(z,0) - WtS_C. \quad (52)$$

1. Numerical method for the carrier flow simulation. The three-dimensional momentum conservation and continuity equations (46)–(49) are solved in a parallelpiped domain $0 \le x \le 2$, $0 \le y \le 1$, $0 \le z \le 1$. Equations (46) and (47) for the fluid phase are discretized in an Eulerian framework using a second-order finite-difference technique on an equispaced staggered grid containing $N_g = 96$ points in each of y- and z-directions and $2N_g = 192$ points in the x-direction. The imposed mean velocity gradient is in the z-direction. The mean advection terms, $Sz\partial_x U_i$, are evaluated using discrete Fourier interpolation. A second order Adams–Bashforth scheme is used to integrate the equations in time with step $\Delta t = 0.5\Delta x$, $\Delta x = 1/N_g$. Pressure is obtained by solving its Poisson equation via a fast Fourier transform in the x- and y-directions and Gaussian elimination in the z-direction. Standard periodic boundary conditions for the velocity components and pressure are imposed in the x- and y-directions. In the z-direction (the direction of the imposed mean velocity gradient) a shear periodic boundary condition is used. The shear periodic boundary condition for any variable $f(t,x,y,z)$ is prescribed as

$$f(t, x + 2m_1, y + m_2, z + m_3) = f(t, x - Sm_3 t, y, z), \quad (53)$$

where m_i are integer numbers. More details about the numerical method and its accuracy are discussed by Gerz *at al.* [19].

We use an initialization algorithm to generate a divergence-free isotropic random fluid velocity field with a prescribed energy spectrum $E(k)$ and spectral cross-correlations matrix

of the velocity, satisfying the realizability constrains [20]. The initial energy spectrum is prescribed by

$$E(k,0) = \frac{3u_0^2}{4\pi}\frac{k}{k_p^2}\exp\left(-\frac{k}{k_p}\right), \tag{54}$$

where u_0 is the dimensionless rms velocity, k is the wave number, $k^2 = k_x^2 + k_y^2 + k_z^2$, where $k_x = 0.5, 1., 1.5, \ldots, N_g/2$, $k_y = 1, 2, \ldots, N_g/2$, $k_z = 1, 2, \ldots, N_g/2$, and k_p is the wave number of peak energy. The wave numbers are normalized by $k_* = 2\pi$. The dimensionless kinematic viscosity ν is calculated from the prescribed initial microscale Reynolds number $Re_{\lambda 0}$ and the computed initial dissipation $\epsilon(0)$.

2. LEM solver for the bubble-laden HSF. In the case of HSF, we perform the integration in two steps. In the first step, we integrate (48) and (49) using LEM solver, without taking into account the mean advection terms, $Sz\partial_x V_i$ and $Sz\partial_x C'$. In the second step, we use Fourier interpolation in evaluating the bubble velocity and concentration at an upstream position where the bubble is advected by the mean velocity Sz (in the x-direction) during the time step dt.

Thus in the first step the LEM solver evaluates the intermediate bubble velocity, $\hat{\boldsymbol{V}}$, and concentration, $\hat{C}$, via solving the following two equations:

$$\frac{d\hat{V}_i}{dt} = 3\left(\frac{DU_i}{Dt} + Sz\partial_x U_i + U_z S\delta_{ix}\right) + \frac{1}{\tau_b}(U_i - V_i + W\delta_{iz}) - V_z S\delta_{ix}, \tag{55}$$

$$\frac{d\hat{C}}{dt} = -(C' + C_0)\partial_j V_j - S_C(V_z - W). \tag{56}$$

In this first step, LEM obtains the intermediate velocity $\hat{\boldsymbol{V}}(\boldsymbol{x_g}, t + dt)$, and concentration $\hat{C}(\boldsymbol{x_g}, t + dt)$, defined on the Eulerian grid.

In the second step (where LEM is not involved), we account for the mean advection terms (second term on lhs of both Eqs. (48) and (49)). Thus we evaluate the bubble velocity, $\boldsymbol{V}$, and concentration, C', at the upstream position from where it is advected by the mean velocity Sz (in the x-direction) during the time step dt using a discrete Fourier interpolation [19] of $\hat{C}(\boldsymbol{x_g}, t + dt)$ and $\hat{\boldsymbol{V}}(\boldsymbol{x_g}, t + dt)$.

DNS of the HSF is performed with the initial parameters $Re_{\lambda 0} = 16$, $u_0 = 0.02$, and $k_p = 6$ (see Eq. (54)), which correspond to an initial dissipation rate $\epsilon(0) = 2.76 \times 10^{-4}$, Taylor microscale $\lambda_0 = 0.0239$, Kolmogorov length scale $\eta_0 = 0.003133$, integral length scale $L_0 = 0.05123$, and kinematic viscosity $\nu = 2.981 \times 10^{-5}$. The dimensionless gravitational acceleration is prescribed $g = 1$. The reference length and time scales used in normalizing the above dimensionless quantities are $L_{ref} = 0.098$ m and $T_{ref} = 0.1$ sec, respectively. The simulation continues to a dimensionless time $t = 8$. In the one-way coupling case, C' is set equal to zero in the last term in Eq. (46), thus eliminating the effects of the bubbles on the carrier flow.

The flow shear number [16], Sh, is defined as

$$Sh = \frac{SE}{\epsilon}, \tag{57}$$

where $E = 0.5\sum_{i=1}^{3}\langle U_i^2\rangle$ is the turbulence kinetic energy, and ϵ is its dissipation rate: $\epsilon = \nu\sum_{i,j=1}^{3}(\partial U_i/\partial x_j)^2$. The shear number equals 2.14 at $t = 0$ and increases to 6.1 at the

end of the simulation, at $t = 8$. Bubbles are injected into the flow at time $t = 0.75$, when the shear number equals $Sh = 2.54$ (denoted as Sh_0 in Figs. 7–13).

Note that the time $t = 8$ equals about $5.5T_e$ (where $T_e \simeq u_0^2/\epsilon$ is the turbulence integral time scale) and $27\tau_k$ (for $\tau_k = 0.31$, the Kolmogorov time scale of the turbulence at $t = 0$). Thus $t = 8$ equals about 27 turn-over times of a dissipative eddy, and the product $Sh_0\, t = 20.32$ (for $t = 8$) is larger than ($Sh\, t_{final} = 14$) in the DNS of HSF reported by Kida and Tanaka [17] and, recently, by Mashayek [18].

Figure 7 shows the temporal development of the turbulence rms velocity components in the x, y, and z directions ($u_1 = \langle U_x^2 \rangle^{1/2}$, $u_2 = \langle U_y^2 \rangle^{1/2}$, and $u_3 = \langle U_z^2 \rangle^{1/2}$), and the dissipation rate of the turbulence kinetic energy, ϵ. The expected anisotropy of turbulence [14–17] is evidenced by the monotonic increase of the horizontal rms velocity components, u_1 and u_2, after the initial decay period, whereas the vertical component, u_3, is suppressed, so that $u_1 > u_2 > u_3$ for $t \geq 0.8$. This anisotropy is consistent with the mechanism of vortex generation described by Kida and Tanaka [17].

Note that the growth rates of the rms velocity and the turbulence energy dissipation rate, ϵ, depend strongly on the shear number, Sh. For $Sh \gg 1$, both u_i and ϵ increase exponentially [16]. In the DNS of HSF by Mashayek [18] with $Sh = 2$, a linear growth of the turbulence kinetic energy, $E = 0.5 \sum_i u_i^2$, is observed for $Sh\, t < 10$, and a slower growth of E at later times. In our DNS (with $Sh_0 = 2.54$), ϵ and u_3 increase for $t \geq 3.7$ (or $Sh_0\, t \geq 9.4$) approximately as t^2 after an initial transient decay, whereas the components u_1 and u_2 grow linearly with time for $t > 2$, so that the turbulence kinetic energy grows as t^2.

Figure 8 shows the temporal development of the Reynolds number, Re_λ, the Kolmogorov length scale η, and skewness of the velocity derivative, Sk, defined as

$$Sk = -\sqrt{3} \sum_{i=1}^{3} \frac{\langle (\partial_i U_i)^3 \rangle}{\left[\langle (\partial_i U_i)^2 \rangle \right]^{3/2}}. \tag{58}$$

The figure shows that, after an initial transient decay, Re_λ increases to a value $\simeq$37 at

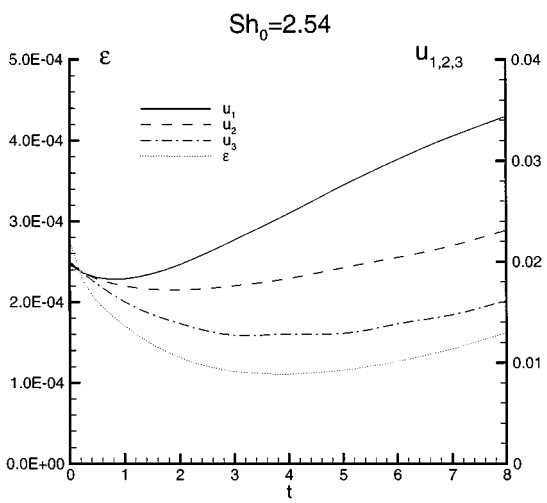

FIG. 7. Temporal development of the turbulence dissipation rate (ϵ) and the rms velocity components ($u_1 = \langle U_x^2 \rangle^{1/2}$, $u_2 = \langle U_y^2 \rangle^{1/2}$, $u_3 = \langle U_z^2 \rangle^{1/2}$) in the homogeneous turbulent shear flow; $t = 8$ corresponds to $Sh_0 t = 20.32$.

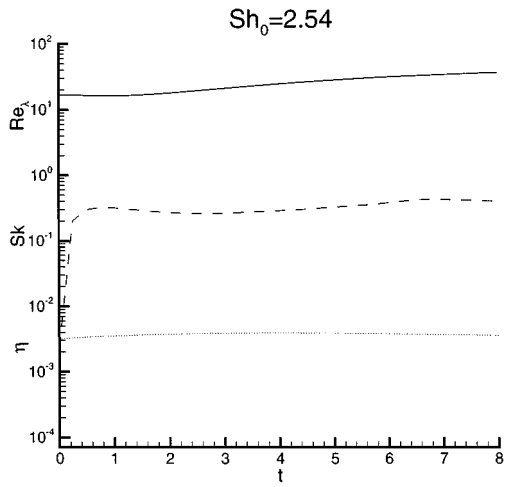

FIG. 8. Temporal development of the turbulence Kolmogorov scale, η (in dotted line), skewness, Sk (in dashed line), and microscale Reynolds number, Re_λ (in solid line), in the homogeneous turbulent shear flow.

$t = 8$. The ability of the simulation to resolve the motion at the smallest turbulence scales is assured by the criterion $\eta k_{max} > 1$, where $k_{max} = N_g \pi$ is the highest resolved wave number for the given grid spacing ($\Delta x = 1/N_g$). In our case, $\eta k_{max} \geq 1.0$ throughout the simulation.

The skewness reaches its first peak, $Sk \simeq 0.326$ at $t = 0.75$, when a fully developed turbulence is established. Therefore, in our DNS we chose $t = 0.75$ as the time of the injection of bubbles into the flow.

The dimensionless bubble diameter $d_b = 0.00242$, and the dimensionless response time $\tau_b \simeq 0.00548$. At the injection time ($t = 0.75$) the Kolmogorov length and time scales are $\eta = 0.003464$ and $\tau_k = 0.3813$, and thus the bubble diameter and response time are $d_b = 0.7\eta$ and $\tau_b \simeq 0.0144\tau_k$; the dimensional bubble diameter is $d_b \simeq 240\,\mu$m. The bubble initial concentration in this simulation is uniform, $C(t = 0.75) = \alpha_0$, and is assumed small enough (e.g., $\alpha_0 = 10^{-4}$) to neglect the influence of the bubbles on the carrier flow. Note that the value of α_0 is relevant only in the two-way coupling case, since Eq. (49) is integrated with C' normalized by α_0. The initial bubble velocity is prescribed as

$$V_i = U_i + W\delta_{iz}, \tag{59}$$

where W is the bubble terminal velocity (34). Our numerical results show that the bubble Reynolds number remains less than 1 throughout the simulation. Therefore, we satisfy the conditions of validity of the bubble equation of motion (48) (cf. [1]).

Figures 9 and 10 show respectively the contours of turbulence enstrophy and bubble concentration in an (x, z)-plane, at $y = 0.5$, at $t = 6$. Figure 9 shows that intense vortex layers are created, inclined at 15° to 30° to the downstream, and dominate the flow field. This flow structure is in agreement with that obtained by Kida and Tanaka from their DNS [17]. In order to ensure that the x-length of the computational domain is large enough to satisfy the imposed periodic boundary condition in the x-direction without artificially distorting the flow structure, we evaluated the two-point instantaneous velocity correlation

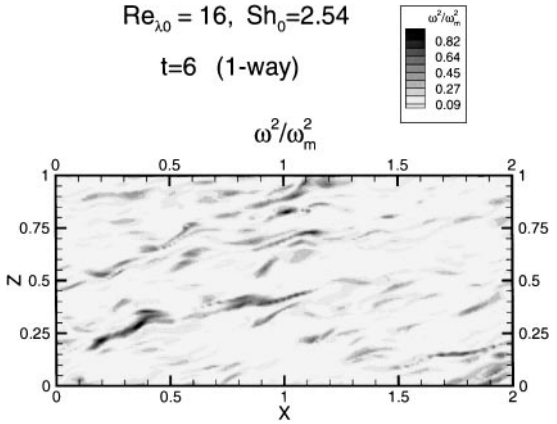

FIG. 9. Contours of the turbulence enstrophy in the homogeneous turbulent shear flow at time $t = 6$, normalized by the maximum value $\omega_m^2 = 32.22$.

coefficients,

$$\langle U_i(x + r_0, y, z, t)U_i(x, y, z, t)\rangle \Big/ \left[\left\langle U_i(x + r_0, y, z, t)^2\right\rangle \left\langle U_i(x, y, z, t)^2\right\rangle\right]^{1/2}$$

as a function of the separation distance in the x-direction, r_0, between the points. Our results show that the velocity correlation coefficients vanish for $r_0 \leq 0.5$, indicating that the vortex structures are not distorted by the (x-) periodic boundary condition.

Figure 10 shows that the bubble-phase concentration becomes non-uniform owing to the preferential accumulation of bubbles in the oblique vortex layers dominating the carrier flow structure.

Figure 11 shows the temporal development of the normalized bubble concentration variance $\langle C'^2\rangle^{1/2}/\alpha_0$, and maximum modulus of the concentration gradient, $|\nabla C|_m/\alpha_0$. The figure shows that $\langle C'^2\rangle$ increases monotonically owing to the bubble accumulation. We also deduce from the figure that the effect numerical diffusion remains negligible and does not degrade the rapid growth of $|\nabla C|_m/\alpha_0$.

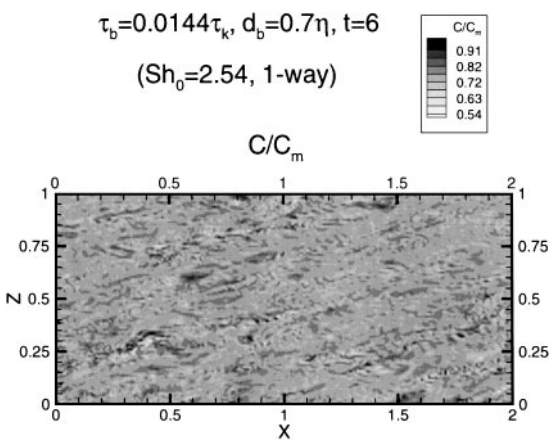

FIG. 10. Contours of the bubble concentration, normalized by the maximum value $C_m = 1.345\alpha_0$ in the homogeneous turbulent shear flow at time $t = 6$. The corresponding turbulence enstrophy field is shown in Fig. 9.

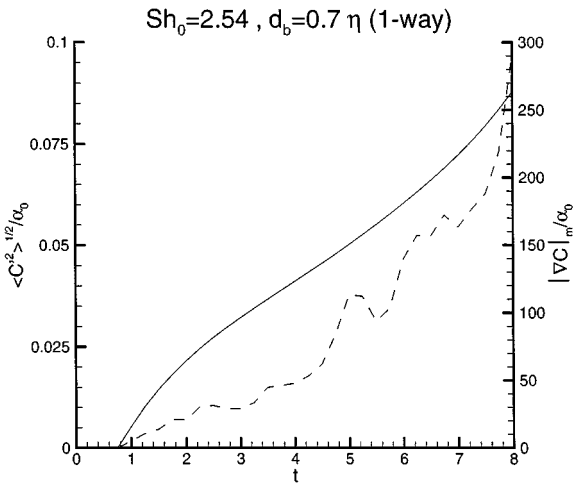

FIG. 11. Temporal development of the bubble concentration variance, $\langle C'^2\rangle^{1/2}/\alpha_0$ (solid line), and the maximum modulus of the concentration gradient, $|\nabla C|_m/\alpha_0$ (dahsed line), normalized by the reference concentration, α_0.

Figure 12 shows a band-averaged spectrum, $E_C(k)$, of the concentration fluctuation defined as

$$E_C(k) = \sum_{k<\boldsymbol{k}<k+1} |C'(\boldsymbol{k}, t)|^2 \tag{60}$$

at time $t = 6$. The figure shows that $E_C(k)$ increases with k owing to the bubble preferential accumulation and the growth of the concentration gradients (cf. Fig. 11) and has no cut-off at high wave numbers. This behavior of $E_C(k)$ confirms that the effects of numerical diffusion in the DNS remain negligible. On the other hand, for the considered time interval ($0 < t < 8$), we do not observe any numerical instability, which would cause an explosive growth of $E_C(k)$ for large k. Such instability may occur at later times due to decreasing

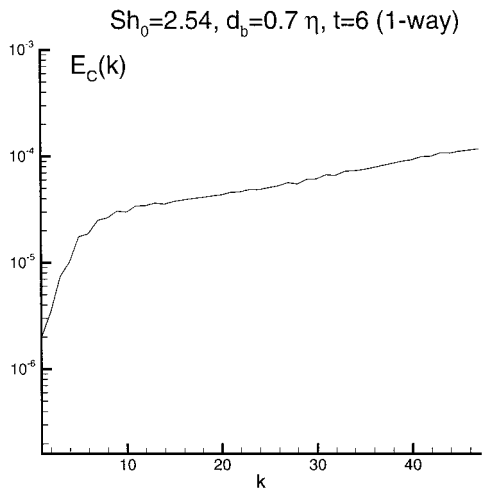

FIG. 12. Spectrum of the bubble concentration fluctuation, E_C.

Kolmogov length scale η and the resulting insufficient resolution (for $k_{max}\eta < 1$). In the present simulation, $k_{max}\eta = 1.08$ at $t = 8$.

In order to examine the performance of LEM in the DNS of HSF with two-way coupling, we consider three cases with different initial bubble concentration profiles in the z-direction, but with the same bubble response time as in the one-way coupling case.

The first case is for a uniform initial bubble concentration,

$$C(t = 0) = \alpha_0, \tag{61}$$

where α_0 is a reference concentration set equal to 5×10^{-3} to neglect bubble–bubble interactions.

The second case is for stable linear stratification, with a constant concentration gradient in the vertical (z) coordinate,

$$C(z, t = 0) = \alpha_0(1 + S_C z), \qquad S_C = 1, \tag{62}$$

while the third case is for unstable linear stratification,

$$C(z, t = 0) = \alpha_0(2 + S_C z), \qquad S_C = -1. \tag{63}$$

In the cases of stable ($S_C = 1$) and unstable ($S_C = -1$) stratification, shear-periodic boundary conditions in the z-direction are imposed on the instantaneous concentration fluctuation $C' = C - C_0(z, t)$, where $C_0(z, t)$ is the instantaneous mean concentration in a given $(x - y)$ plane. The simulation is continued to $t = 6$.

Figure 13 shows the temporal development of the turbulence kinetic energy relative difference $(E_{2w} - E_{1w})/E_{1w}$ due to the two-way coupling (where the subscripts $2w$ and $1w$ denote respectively two-way and one-way coupling). The figure shows that, as expected [1], $E_{2w}(t)$ is reduced compared to $E_{1w}(t)$ in the case of stable stratification and increased for unstable stratification. In the non-stratified case, the modification of $E(t)$ compared to the one-way coupling case is negligible.

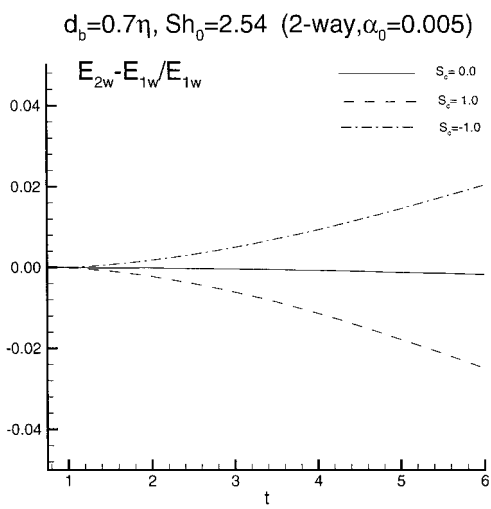

FIG. 13. Temporal development of the modification of the turbulence kinetic energy in the homogeneous turbulent shear bubble-laden flow.

In the simulations with both one- and two-way coupling, the volume integral of C over the computational domain is conserved with accuracy $\simeq 0.2\%$. A typical run until time $t = 8$ of the DNS using TF-LEM solver takes one CPU-hour on Cray-T90. This is at least one order of magnitude less than the amount of CPU-time required for the same simulation using the trajectory approach.

IV. CONCLUDING REMARKS

We have developed a Lagrangian–Eulerian mapping solver (LEM) for direct numerical simulations (DNS) of particle-laden turbulent flows using the two-fluid formulation (TF). The motivation for using TF in DNS of particle-laden flows is that it reduces significantly the required CPU-time and storage memory, as compared to the trajectory approach [2].

In order validate the new method, we performed DNS with TF-LEM of three different flows: a bubble-laden Taylor–Green vortex, a two-dimensional, spatially developing mixing layer, and a three-dimensional homogeneous shear turbulent flow. The results show that LEM is superior to the standard finite-difference scheme (FDS) for the intergation of the equations for the bubble velocity and concentration. In the case of sufficiently large bubbles (i.e., whose response time is large enough), FDS is not capable of resolving the large gradients of the bubble-phase velocity and concentration. These gradients are created by nonlinear advection as well as preferential accumulation, causing the development of numerical instability in the absence of *any* diffusion terms in the equations of motion of the bubble phase. In contrast, LEM resolves the gradients of the velocity and concentration without creating numerical instability, even if the bubbles added-mass inertia is significant and their preferential accumulation is well pronounced.

ACKNOWLEDGMENTS

This work was supported by ONR Grant N00014-96-1-0213 administered by Dr. E. Rood, and by NASA Grant NAG3-1831 administered by Dr. K. Hsieh. The computations were performed on Cray T90 located at the Naval Oceanographic Center, Mississippi.

REFERENCES

1. O. A. Druzhinin and S. E. Elghobashi, Direct numerical simulations of bubble-laden turbulent flows using the two-fluid formulation, *Phys. Fluids* **10**, 685 (1998).
2. S. E. Elghobashi, On predicting particle-laden turbulent flows, *Appl. Sci. Res.* **52**, 309 (1994).
3. M. R. Maxey, The motion of small spherical particles in a cellular flow field, *Phys. Fluids* **30**, 1915 (1987).
4. L.-P. Wang and M. R. Maxey, Settling velocity and concentration distribution of heavy particles in homogenous isotropic turbulence, *J. Fluid Mech.* **256**, 27 (1993).
5. J. K. Eaton and J. R. Fessler, Preferential concentration of particles by turbulence, *Int. J. Multiphase Flow* **20**, 169 (1994).
6. J. C. Tannehill, D. A. Anderson, and R. H. Pletcher, *Computational Fluid Mechanics and Heat Transfer*, 2nd ed. (Taylor & Francis, Washington, 1997), p. 177.
7. G. I. Taylor, On the decay of vortices in a viscous fluid, *Philos. Mag.* **46**, 671 (1923).
8. O. A. Druzhinin and S. E. Elghobashi, Direct numerical simulation of a three-dimensional spatially-developing turbulent bubble-laden mixing layer with two-way coupling, submitted.
9. P. S. Lowery and W. C. Reynolds, *Numerical Simulation of a Spatially-Developing, Forced, Plane Mixing Layer*, Report No. TF-26, Mech. Eng. Department, Stanford University, Stanford, CA, September 1986.

10. R. Wilhelmson and J. Ericksen, Direct solution for Poisson's equation in three dimensions *J. Comput. Phys.* **25**, 319 (1977).
11. U. Schumann and R. A. Sweet, Fast Fourier transforms for direct solution of Poisson's equation with staggered boundary conditions, *J. Comput. Phys.* **75**, 123 (1988).
12. H. Schmidt, U. Schumann, and H. Volker, *Three-Dimensional, Direct and Vectorized Elliptic Solvers for Various Boundary Conditions*, Report DFVLR-Mitt. 84-15, 1984.
13. N. D. Sandham and W. C. Reynolds, Some inlet plane effects on the numerically simulated spatially developing two-dimensional mixing layer, in *Turbulent Shear Flows* (Springer-Verlag, New York, 1989), Vol. 6, p. 441.
14. F. H. Champagne, V. G. Harris, and S. Corrsin, Experiments on nearly homogeneous turbulent shear flow, *J. Fluid Mech.* **41**, 81 (1970).
15. S. Tavoularis and U. Karnik, Further experiments on the evolution of turbulent stresses in uniformly sheared turbulence, *J. Fluid Mech.* **204**, 457 (1989).
16. S. Kida and M. Tanaka, Reynolds stress and vortical structure in a uniformly sheared turbulence, *J. Phys. Soc. Jpn.* **61**, 4400 (1992).
17. S. Kida and M. Tanaka, Dynamics of vortical structures in a homogeneous shear flow, *J. Fluid Mech.* **274**, 43 (1994).
18. F. Mashayek, Droplet-turbulence interactions in low-Mach-number homogeneous shear two-phase flows, *J. Fluid Mech.* **367**, 163 (1998).
19. T. Gerz, U. Schumann, and S. Elghobashi, Direct simulation of stably stratified homogeneous turbulent shear flows, *J. Fluid Mech.* **200**, 563 (1989).
20. U. Schumann, Realizability of Reynolds-stress turbulence models, *Phys. Fluids* **20**, 721 (1977).